Thermal constraints on the reionization of hydrogen by Population II stellar sources

Sudhir Raskutti,[1]* James S. Bolton,[1] J. Stuart B. Wyithe[1,2] and George D. Becker[3]

[1]*School of Physics, University of Melbourne, Parkville, VIC 3010, Australia*
[2]*ARC Centre of Excellence for All-sky Astrophysics (CAASTRO), School of Physics A28, The University of Sydney, NSW 2006, Australia*
[3]*Kavli Institute for Cosmology and Institute of Astronomy, Madingley Road, Cambridge CB3 0HA*

ABSTRACT

Measurements of the intergalactic medium (IGM) temperature provide a potentially powerful constraint on the reionization history due to the thermal imprint left by the photoionization of neutral hydrogen. However, until recently IGM temperature measurements were limited to redshifts $2 \leq z \leq 4.8$, restricting the ability of these data to probe the reionization history at $z > 6$. In this work, we use recent measurements of the IGM temperature in the near-zones of seven quasars at $z \sim 5.8$–6.4, combined with a semi-numerical model for inhomogeneous reionization, to establish new constraints on the redshift at which hydrogen reionization completed. We calibrate the model to reproduce observational constraints on the electron scattering optical depth and the H I photoionization rate, and compute the resulting spatially inhomogeneous temperature distribution at $z \sim 6$ for a variety of reionization scenarios. Under standard assumptions for the ionizing spectra of Population II sources, the near-zone temperature measurements constrain the redshift by which hydrogen reionization was complete to be $z_r > 7.9$ (6.5) at 68 (95) per cent confidence. We conclude that future temperature measurements around other high-redshift quasars will significantly increase the power of this technique, enabling these results to be tightened and generalized.

Key words: intergalactic medium – quasars: absorption lines – cosmology: observations – dark ages, reionization, first stars.

1 INTRODUCTION

The reionization of cosmic hydrogen represents a significant moment in the history of the Universe. The appearance of the first stars and quasars heated and ionized the intergalactic medium (IGM), catalysing the transition in which intergalactic hydrogen changed from being predominantly neutral to its present-day, highly ionized state. Understanding exactly how and when this phase transition occurred will offer insight into the nature of the first sources of light (e.g. Barkana & Loeb 2001). However, existing constraints on the time-scale and extent of reionization are currently uncertain (Choudhury & Ferrara 2006; Pritchard et al. 2010; Mitra, Choudhury & Ferrara 2011).

There are two primary observations which are used to constrain the epoch of hydrogen reionization. The first of these is the absorption spectra of quasars at $z \simeq 6$ (White et al. 2003; Fan 2006; Becker, Rauch & Sargent 2007). These enable detailed study of the IGM ionization state at high redshift, and indicate that the Universe was reionized at $z \geq 6$ (Gnedin & Fan 2006, but see also Mesinger

2010). The second observation is provided by measurements of the Thomson optical depth, τ_{CMB}, to the surface of last scattering, which indicate that hydrogen reionization could not have ended any earlier than $z_r = 10.6 \pm 1.2$ (Komatsu et al. 2011). In practice, this constraint is consistent with a wide variety of extended reionization scenarios.

Analytical and semi-numerical models have been confronted with a combination of these and other observations to place more quantitative limits on the reionization redshift. In particular, studies by Choudhury & Ferrara (2006), Pritchard et al. (2010) and Mitra et al. (2011) employ the above observables, alongside the observed distribution of Lyman limit systems and constraints on the star formation rate, to model reionization. These models can be used to infer constraints on the extent and completion time of reionization. However, lack of direct observational evidence at $z > 6$ means that parameters in these models, such as the ionizing background intensity and the thermal state of the IGM, are relatively uncertain at high redshift. This implies that, from current observations alone, constraints on the redshift by which reionization is complete remain loose, and cannot be improved beyond $6 < z_r < 10.5$ (Mitra et al. 2011).

A promising additional approach comes from measurements of the IGM temperature (Zaldarriaga, Hui & Tegmark 2001; Trac,

*E-mail: s.raskutti@gmail.com

Cen & Loeb 2008; Furlanetto & Oh 2009; Bolton et al. 2010). The relatively long time-scale of adiabatic cooling implies that the low-redshift IGM still carries the thermal imprint of reionization heating from much earlier times. Several authors have previously used this fact, combined with temperature measurements at $z < 4$, to constrain the end of the hydrogen reionization epoch to $z_r < 10$ (Theuns et al. 2002; Hui & Haiman 2003). Unfortunately, because the imprint of reionization heating at $z_r > 10$ reaches a thermal asymptote by $z \approx 4$, these studies are limited by the relatively low redshift at which the temperature measurements were made.

Measurements of the IGM temperature at higher redshift therefore offer a new opportunity to tighten these constraints. A first step towards this was made by Bolton et al. (2010), who obtained a measurement of the IGM temperature at mean density from Lyα absorption lines in the near-zone of the $z = 6.02$ quasar SDSS J0818+1722. Although the statistical uncertainty on their single line-of-sight measurement was large, Bolton et al. (2010) were nevertheless able to use a simple cooling argument to infer a reionization redshift of $z_r < 9$ (to 68 per cent confidence) within the quasar near-zone, assuming hydrogen was reionized by Population II stars. Recently, Bolton et al. (2012) have significantly extended these observational constraints by measuring the IGM temperature in the near-zones of six further quasars at $5.8 \leq z \leq 6.4$. In this work, we therefore seek to extend the modelling of Bolton et al. (2010) and include all seven near-zone temperature measurements to obtain a limit on the *reionization redshift for the general IGM*. Specifically, by using a semi-numerical model to follow inhomogeneous reionization and photoheating of intergalactic hydrogen by stellar sources, as well any subsequent photoheating by the quasar itself, we may calculate near-zone temperatures as a function of spatial position and reionization redshift. A comparison of our model with the observational data then allows us to constrain the redshift at which reionization completed.

This paper is organized as follows. We begin in Section 2 by introducing our semi-numerical model of reionization, and proceed in Section 3 to give a more detailed description of the modelling of ionizing sources. Predicted temperatures from the model for different reionization scenarios are then described in Section 4, and we compare these to the Bolton et al. (2012) quasar temperature measurements. Our constraints on the reionization history are then discussed in Section 5, where we also assess the prospects for improving on these constraints in the future using additional quasar sight-lines. Conclusions and further directions are then presented in Section 6. Throughout this paper, we use Λ cold dark matter cosmological parameters $\Omega_m = 0.27$, $\Omega_\Lambda = 0.73$, $\Omega_b\, h^2 = 0.0225$, $h = 0.704$, $\sigma_8 = 0.81$, $n_s = 0.96$, consistent with recent studies of the cosmic microwave background (CMB; Komatsu et al. 2011).

2 SEMI-NUMERICAL REIONIZATION MODEL

Our model of inhomogeneous hydrogen reionization simulates both the evolving ionization state of the IGM and its thermal history. The former is calculated using the semi-numerical model developed by Wyithe & Loeb (2007) and Geil & Wyithe (2008) (see also Zahn et al. 2007; Mesinger & Furlanetto 2007; Choudhury, Haehnelt & Regan 2009; Thomas et al. 2009, for similar approaches). The ionization state derived from this model is then used to evaluate both the ionizing flux and the mean free path at the Lyman limit, and to infer a temperature distribution for the IGM.

2.1 Ionization model

We simulate the IGM inside a periodic, cubic grid of side-length $L = 100\, h^{-1}$ Mpc, containing $N = 256$ voxels per side-length, with an overdensity field $\delta(x)$ generated using the transfer function of Eisenstein & Hu (1999). The calculations detailing the evolution of ionization structure in this density field (which is initialized to a neutral state at $z = 99$) are described in Geil & Wyithe (2008). Briefly, the model evaluates the ionization fraction $Q_{\delta_R, R}$ of a spherical region of scale R around a given voxel at redshift z as

$$\frac{dQ_{\delta_R, R}}{dt} = \frac{N_{\rm ion}}{0.76} \left[Q_{\delta_R, R} \frac{dF_{\rm col}(\delta_R, R, z, M_{\rm ion})}{dt} \right.$$
$$\left. + \left(1 - Q_{\delta_R, R}\right) \frac{dF_{\rm col}(\delta_R, R, z, M_{\rm min})}{dt} \right]$$
$$- \alpha_B C n_H^0 \left[1 + \delta_R \frac{D_1(z)}{D_1(z_{\rm obs})} \right] (1 + z)^3\, Q_{\delta_R, R}, \qquad (1)$$

where δ_R is the region's overdensity, α_B is the case B recombination coefficient and C is the clumping factor. In this work, we shall assume $C = 3$, broadly consistent with recent results from hydrodynamical simulations (Pawlik, Schaye & van Scherpenzeel 2009; Raičević & Theuns 2011). The justification for this choice, as will be discussed in more detail in Section 5.1, is that it tends to provide the weakest overall constraints on reionization redshift. Meanwhile, $N_{\rm ion}$, the number of ionizing photons entering the IGM per baryon in galaxies, is left as a free parameter, the modelling of which will be described in more detail in Section 3.

The production rate of ionizing photons is then assumed to be proportional to $N_{\rm ion}$ and the rate of change of the collapsed fraction, $F_{\rm col}$, in haloes above some minimum threshold mass for star formation ($M_{\rm min}$ in neutral and $M_{\rm ion}$ in ionized regions, corresponding to virial temperatures of 10^4 and 10^5 K, respectively, e.g. Dijkstra et al. 2004). The collapsed fraction in a region of comoving radius R and mean overdensity $\delta(z) = \delta(z_{\rm obs}) D_1(z)/D_1(z_{\rm obs})$ is found using the extended Press–Schechter model (Bond et al. 1991), which gives

$$F_{\rm col}(\delta_R, R, z) = {\rm erfc} \left[\frac{\delta_c - \delta_R(z)}{\sqrt{2(\sigma_{\rm gal}^2 - \sigma_R^2)}} \right], \qquad (2)$$

where ${\rm erfc}(x)$ is the complementary error function, σ_R^2 is the variance of the overdensity field smoothed on a scale R and $\sigma_{\rm gal}^2$ is the variance of the overdensity field smoothed on a scale $R_{\rm gal}$, corresponding to a mass scale of $M_{\rm min}$ or $M_{\rm ion}$ (both evaluated at redshift z).

Equation (1) is solved at every voxel on a range of scales from L to L/N at logarithmic intervals of width $\Delta R/R = 0.1$. A voxel is then deemed to be ionized if it lies inside a region for which $Q_{\delta_R, R} > 1$ on any scale R. By repeating this procedure at successive redshifts, we obtain our ionization field as a function of z.

2.2 The ionizing emissivity

In order to compute the heating of the IGM, we must next obtain the ionizing emissivity in each voxel of our simulation. We simulate the ionization field at 30 regular redshift intervals between an initial redshift, z_0, and the reionization redshift, z_r. These are, respectively, the redshifts corresponding to $Q = 0.01$ and 1.0, where $Q = Q_{\delta_R, R}$ for the case where equation (1) is solved at mean density and $R \to \infty$. At each interval, if a voxel is flagged as ionized, we compute the intrinsic emissivity as the product of $N_{\rm ion}$ and the collapsed fraction above a minimum halo mass, $M_{\rm ion}$. Using this, the proper ionizing photon production rate ($\dot{N}_\gamma$) in units of photons

cm^{-3} s^{-1}, at each voxel, is

$$\dot{N}_\gamma = \frac{\rho_c \Omega_b (1+z)^3 (1+\delta_\lambda) N_{ion}}{\mu m_p} \frac{dF_{col}(\delta_\lambda, \lambda_{HI}, z, M_{ion})}{dt}, \quad (3)$$

where ρ_c is the present-day critical density, m_p is a proton mass and μ is the mean molecular weight. In this instance, the smoothing scale λ used to calculate the collapsed fraction is given by the minimum of the ionized bubble radius and the mean free path at the Lyman limit, λ_{HI}. This is related to the ionizing emissivity ϵ_ν (in units of erg s^{-1} cm^{-3} Hz^{-1}) above the Lyman Limit frequency, ν_{HI}, by

$$\dot{N}_\gamma = \int_{\nu_{HI}}^\infty \frac{\epsilon_\nu}{h_p \nu} \, d\nu, \quad (4)$$

where we adopt a simple power-law spectrum

$$\epsilon_\nu = \left(\frac{\nu}{\nu_{HI}}\right)^{-\alpha} \times \begin{array}{ll} \epsilon_{HI} & (\nu_{HI} \le \nu < \nu_{HeII}), \\ 0 & (\nu_{HeII} \le \nu). \end{array} \quad (5)$$

Here ϵ_{HI} is the emissivity at the hydrogen Lyman limit. Below the He II ionization edge, we take a spectral index of $\alpha = 3$ characteristic of soft, Population II stellar sources (e.g. Hui & Haiman 2003; Furlanetto & Oh 2009). Above ν_{HeII}, the spectrum is zero in order to enforce the requirement that there be no significant stellar ionization of He II. This is necessary for consistency with our semi-numerical reionization model which only traces the propagation of hydrogen ionization fronts, and so cannot predict the larger, extended He III fronts resulting from harder He II ionizing photons. On the other hand, this is not an unrealistic requirement, since the double reionization of helium is thought to not complete until $z \sim 3$ when the number density of quasars is at its peak (Madau & Meiksin 1994; Wyithe & Loeb 2003; Furlanetto & Oh 2008). Nevertheless, this assumption rules out the consideration of more exotic ionization models involving early populations of quasars or Population III sources, which could produce different thermal histories. More detailed modelling, which accounts for doubly ionized helium, may therefore be performed in the future. In this work, however, we consider *hydrogen reionization by Population II stellar sources only*.

2.3 The ionizing background specific intensity

Having computed the intrinsic emissivity, the specific intensity, J_ν, at each voxel may then be calculated by accounting for the propagation and attenuation of radiation. This is a complicated calculation since, in general, it depends on the topology of H II regions around each point in the simulation and the distribution of Lyman limit systems. A full numerical evaluation therefore requires radiative transfer, which is not included in our model. Fortunately, the long-term thermal evolution (for time-scales longer than the local photoionization time-scale) is relatively insensitive to the exact amplitude of J_ν, and instead depends primarily on the spectral shape of the ionizing radiation (Hui & Haiman 2003; Bolton, Oh & Furlanetto 2009). Therefore, to estimate the specific intensity we make the simplifying assumption that the mean free path is much smaller than the horizon scale, and use the local source approximation (e.g. Faucher-Giguère et al. 2009). We compute the mean free path in two regimes, prior to and following overlap of H II regions.

Prior to overlap, the mean free path is set by the size of H II bubbles (Gnedin & Fan 2006), and may therefore be found by partitioning the ionization field into approximately spherical H II regions. To do this, we smooth over the ionization field at successive scales, employing the same logarithmic descent as for our density field. At each scale, we calculate the size of discontiguous regions with

a standard Friend-of-Friends (FoF) algorithm. The bubble size for each voxel is then the scale of the smallest FoF region of which it is part, augmented by the smoothing scale. This has the effect of dividing bubbles that only barely overlap into separate spheres so that the spherical approximation remains valid to a filling factor of around $Q \approx 0.5$. We then assume that the optical depth to ionizing photons is infinite beyond the H II region radius. Lyman limit photons therefore travel one mean free path, corresponding to the H II region size, before being absorbed.

In the post-overlap case, the IGM is fully ionized and the mean free path of H I ionizing photons is constrained by the abundance of Lyman limit systems rather than the sizes of H II regions. In this instance, we employ a fit to the mean free path at the Lyman limit in proper Mpc, taken from Songaila & Cowie (2010):

$$\lambda_{HI} = \frac{88.6}{\Gamma(2-\beta)} \left(\frac{1+z}{4.5}\right)^{-4.44} \text{Mpc}, \quad (6)$$

where Γ denotes the gamma function, and β is the power-law exponent of the H I column density distribution. Observationally, the value of this exponent is unconstrained at $z > 6$, however, at lower redshift measurements indicate $\beta \approx 1.5$ (Petitjean et al. 1993; Hu et al. 1995). Since this is roughly constant over the range $2 < z < 4$ (Misawa et al. 2007), we simply extrapolate to high redshift and adopt $\beta = 1.5$ throughout. We note that the column density distribution will change significantly as we enter the reionization epoch; however, as we are primarily interested in the value of β in the post-overlap regime, this does not affect our results. Finally, we assume that a given H II region is in the pre-overlap regime if its radius is less than λ_{HI} (i.e. the mean free path is not set by Lyman limit systems) and is in the post-overlap regime otherwise.

Adopting the local source approximation, the ionizing background specific intensity in each voxel may then be approximated by

$$J_\nu \simeq \frac{1}{4\pi} \epsilon_\nu \lambda_\nu, \quad (7)$$

where $\lambda_\nu = \lambda_{HI}(\nu/\nu_{HI})^{3(\beta-1)}$. Prior to overlap λ_{HI} is fixed to the H II region size, while post-overlap it is given by equation (6). Finally, note that in both regimes at frequencies above the Lyman limit, we have $J_\nu \propto \nu^{-\alpha+3(\beta-1)}$. This effectively hardens the intrinsic stellar spectrum by $\alpha \to \alpha - 1.5$, accounting for the additional heating due to filtering of the ionizing radiation by discrete, Poisson distributed absorbers in the intervening IGM (e.g. Miralda-Escudé 2003; Faucher-Giguère et al. 2009).

2.4 The thermal evolution

Once the specific intensity at a given voxel is known, the photoionization rates, Γ_i (s^{-1}), and photoheating rates, g_i (erg s^{-1}), for $i = $ H I, He I and He II, may be calculated via

$$\Gamma_i = \int_{\nu_i}^\infty \frac{4\pi J_\nu}{h_p \nu} \sigma_i(\nu) \, d\nu, \quad (8)$$

$$g_i = \int_{\nu_i}^\infty \frac{4\pi J_\nu}{h_p \nu} h_p(\nu - \nu_i) \sigma_i(\nu) \, d\nu, \quad (9)$$

where $\sigma_i(\nu)$ and ν_i are the photoionization cross-section and frequency at the ionization edge for species i, respectively. The temperature evolution is then computed by solving

$$\frac{dT}{dt} = \frac{(\gamma-1)\mu m_p}{k_B \rho} [G(t) - \Lambda(t, n_i)] - 2H(t)T + \frac{T}{\mu} \frac{d\mu}{dt}, \quad (10)$$

where $\gamma = \frac{5}{3}$, and $G = \sum_i n_i g_i$ and Λ are the total photoheating and cooling rates per unit volume, respectively. We ignore any heating resulting from the growth of density fluctuations as this is a minimal effect throughout the short time-scale of reionization. Our code for solving equation (10) follows photoionization and heating, collisional ionization, radiative cooling, Compton cooling and adiabatic cooling for six species (H I, H II, He I, He II, He III and e$^-$). The non-equilibrium abundances of these species are found by additionally solving three further differential equations coupled to equation (10) (e.g. Anninos et al. 1997; Bolton & Haehnelt 2007), and taking a uniform clumping factor of $C = 3$ for all species. We use the rates compiled in Bolton & Haehnelt (2007) with the exception of the case B recombination and cooling rates of Hui & Gnedin (1997) and the photoionization cross-sections of Verner et al. (1996). The gas density, ρ, is evaluated from our linear overdensity field using a standard lognormal fit (Coles & Jones 1991), which approximates the real non-linear density for the majority of voxels. Whilst this does not adequately reproduce the extreme overdense and underdense tails of the density distribution (Becker et al. 2007), its use does not represent a significant source of error since the temperature measurements we compare to are smoothed over the measured quasar near-zones ($\sim$5 proper Mpc). Inaccuracies in evaluating the thermal history of the small number of regions that fall within these tails are therefore unimportant.

Using this prescription, we evolve the temperature of each voxel, independent of all others from an initial temperature $T_0 = 2.27(1 + z)$ K and an initially neutral state. This procedure yields a final temperature distribution over our simulation volume as a function of redshift.

2.5 Inclusion of quasar He II photoheating

The final part of our model is including the effect of the quasars themselves on the thermal state of the IGM in their vicinity. The ionizing flux from a quasar will significantly alter the thermal state of the surrounding IGM, as its harder, non-thermal spectrum will also reionize He II (Bolton et al. 2010). For any given quasar from Bolton et al. (2012), placed in the simulation volume at a random position, we account for this heating by augmenting the specific intensity in each voxel within the quasar proximity-zone by an additional term

$$J_{\nu,q} \simeq \frac{L_\nu}{(4\pi R)^2} \exp\left[-\frac{R}{\lambda_{\rm HI}}\left(\frac{\nu}{\nu_{\rm HI}}\right)^{-3(\beta-1)}\right], \tag{11}$$

where R is the proper distance from the quasar and $L_{\nu,q} = L_{\rm HI,q}(\nu/\nu_{\rm HI})^{-\alpha_q}$ is the quasar ionizing luminosity, again taken to be a power-law spectrum with index α_q. There is considerable uncertainty concerning the exact value of this exponent towards high redshift. We therefore allow it to vary over the range $1.0 \le \alpha_q \le 2.0$, which is consistent with recent indirect estimates from observations of quasar near-zone sizes at $z > 6$ (Wyithe & Bolton 2011). To compute the quasar luminosities at the Lyman limit, we take the absolute AB magnitudes from Carilli et al. (2010). Finally, we fix the extent of the region which experiences additional ionization and heating by each quasar to 5 proper Mpc, matching the radius within which the near-zones were analysed in Bolton et al. (2012).

3 MODELLING OF IONIZING SOURCES

We next discuss the parametrization of ionizing sources in our model, encapsulated by the redshift-dependent parameter $N_{\rm ion}$, the

Table 1. Photoionization rate constraints from the Lyα forest opacity obtained by Bolton et al. (2005) and Wyithe & Bolton (2011). The most likely derived value and errors at 68 per cent confidence intervals for the corresponding number of ionizing photons entering the IGM per baryon in galaxies, $N_{\rm ion}$, are also given.

Redshift	Γ_{-12}	$N_{\rm ion}$
4	$0.97^{+0.48}_{-0.33}$	$35.3^{+17.5}_{-12.1}$
5	$0.47^{+0.3}_{-0.2}$	$22.7^{+14.3}_{-9.7}$
6	$0.18^{+0.18}_{-0.09}$	$13.0^{+13.0}_{-6.5}$

number of ionizing photons entering the IGM per baryon in galaxies. We begin by describing existing observational constraints on the IGM ionization state and then proceed to discuss how these are used to calibrate $N_{\rm ion}$ and its evolution with redshift.

3.1 Observational constraints on $N_{\rm ion}$

3.1.1 The ionization rate from the Lyα forest opacity

Observations of the Lyα forest in quasar absorption spectra can be used to infer the ionizing background due to luminous sources. The measured quantity is the mean transmission of Lyα flux, $\langle F \rangle$, along the line of sight, or equivalently the effective optical depth $\tau_{\rm eff} = -\log\langle F \rangle$. With knowledge of the physical properties of the IGM, these can be converted into the background photoionization rate per hydrogen atom ($\Gamma_{\rm HI} = \Gamma_{-12} \times 10^{-12}$ s^{-1}). Using full hydrodynamical simulations of the IGM, Bolton et al. (2005) and Wyithe & Bolton (2011) have measured Γ_{-12} from the Lyα forest opacity at $z = 4$–6. Their derived values are shown in Table 1. These measurements may then be compared to our own simulated ionization rate, which is calculated using equation (8). When combined with equations (3)–(7), and evaluated for the case of a uniformly ionized IGM at $z < 6$, this yields constraints on $N_{\rm ion}$, which are also shown in Table 1.

3.1.2 Thomson optical depth to CMB photons

The electron scattering optical depth provides an integrated constraint on the IGM ionization state throughout the epoch of reionization. We use results from the latest *WMAP* observations, $\tau_{\rm CMB} = 0.088 \pm 0.015$ (Komatsu et al. 2011). This is related to the ionization history by

$$\tau_{\rm CMB} = \int_0^{z_{\rm CMB}} c\frac{{\rm d}t}{{\rm d}z} Q(z)\left[1 + f_{\rm He}(z)\right] n_{\rm H}(z)\sigma_{\rm T}\,{\rm d}z, \tag{12}$$

where $\sigma_{\rm T}$ is the Thomson scattering cross-section, $n_{\rm H}$ is the hydrogen number density and $f_{\rm He}$ is a correction factor due to the presence of ionized helium. In our model, we assume that the ionization of He I traces that of H I, whilst He II is instantaneously ionized at $z = 3$.

3.2 Parametrization of $N_{\rm ion}$

Using these observations, we may now constrain possible parametrizations of $N_{\rm ion}$ in our model. There is considerable uncertainty concerning the exact shape of $N_{\rm ion}$, particularly for $z > 6$, where there are no direct observations. Indeed, several studies (Pritchard et al. 2010; Mitra et al. 2011) have found that $N_{\rm ion}$ is effectively unconstrained in the range $6 < z < 11$. To explore the

sensitivity of our simulated temperatures to changes in the ionizing sources, we therefore choose to employ two different models for the redshift evolution of N_{ion}.

3.2.1 Linear model

The simplest model, and one often used in previous simulations of reionization (e.g. Haiman & Loeb 1997; Geil & Wyithe 2008), assumes a single, redshift-independent parametrization of N_{ion}. However, this cannot be reconciled with measurements of the photoionization rate from the Lyα forest at $z \le 6$, so we employ a slight variant on the model. We take N_{ion} to be a constant up to the reionization redshift, which is found by solving equation (1) for a universe that is fully ionized by the desired redshift. This effectively fixes the reionization history for any given z_r. Then, to ensure consistency with observations of Γ_{-12}, we allow $N_{ion}(z)$ to evolve linearly once reionization is complete in order to best fit the data points at $z < 6$. This is broadly consistent with predicted increases in the escape fraction towards high redshift (Wyithe et al. 2010). As part of our constraint on z_r, we impose the resulting electron scattering optical depth as an a posteriori constraint on z_r alongside the predicted temperatures in Section 5.

3.2.2 Cubic model

We also explore arbitrary ionization histories that best match the τ_{CMB} constraint, by employing a model that is redshift-dependent

prior to z_r. To ensure enough freedom to match all constraints, we choose to follow the approach of Pritchard et al. (2010) and model N_{ion} as a cubic function, allowing for a large variety of different evolutions:

$$N_{ion}(z) = (N_p - N_0) \left[4 \left(\frac{z - z_0}{\Delta z} \right)^3 - 3 \left(\frac{z - z_0}{\Delta z} \right) \right] + N_0, \quad (13)$$

where we have parametrized by the mid-point (z_0, N_0), and the peak $\left(z_0 + \frac{\Delta z}{2}, N_p \right)$. For each reionization redshift, we fit this curve to the measured electron scattering optical depth and the ionization rate at $z = 4$–6. As in Pritchard et al. (2010), we impose a prior on the comoving emissivity of $\dot{N}_\gamma < 10^{51}$ s^{-1} Mpc^{-3} to disallow unphysically large ionizing backgrounds. We stress that this model is not physically motivated and clearly overfits the limited data we use. However, as we do not seek to exactly find N_{ion} but only to view the effect of different ionization histories on simulated IGM temperatures, this does not significantly impact upon our results.

3.2.3 Optimal N_{ion} models

Finally, the best-fitting evolution of N_{ion} and the filling factor Q for the cubic and linear models are shown in Fig. 1 for $z_r = 6.5$ and 9.0. For both cases, the behaviour of the emissivity matches quite well to results derived elsewhere (Choudhury & Ferrara 2006; Pritchard et al. 2010; Mitra et al. 2011), although note that for early reionization in the cubic model, star formation switches on later and the
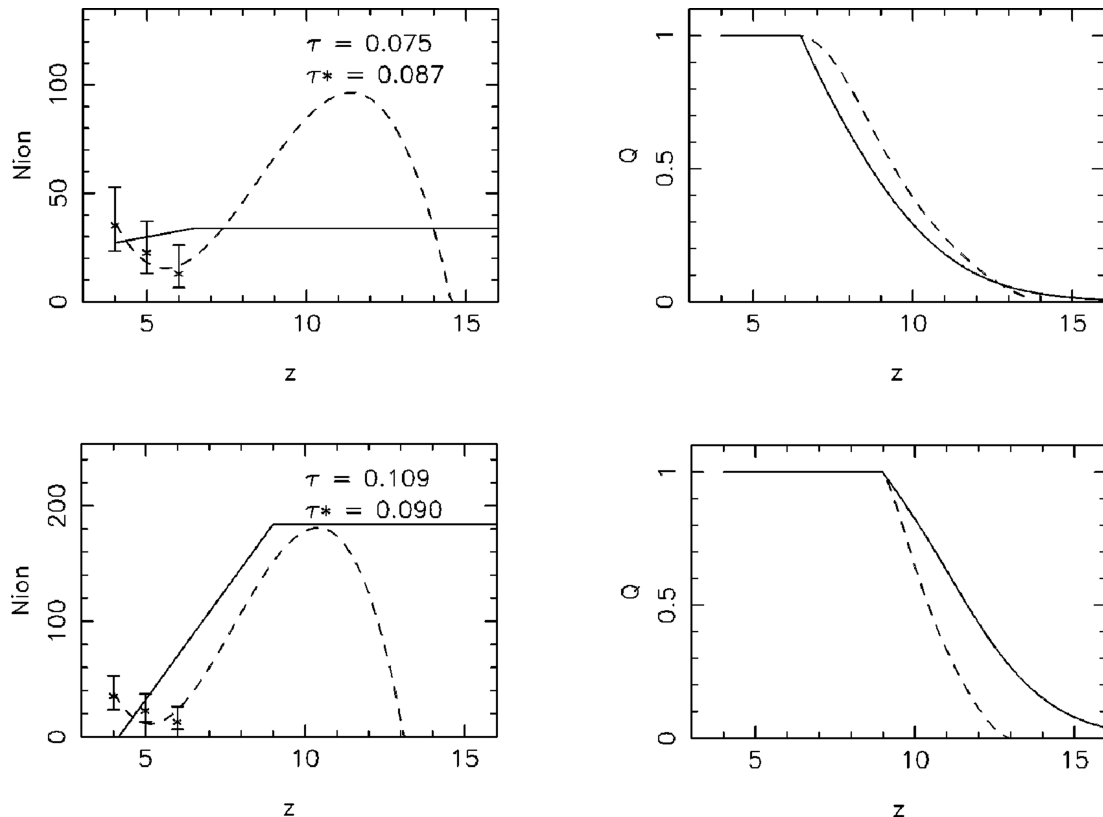

Figure 1. Evolution of the number of ionizing photons per baryon in galaxies which escape into the IGM, N_{ion} (left-hand column), and the H II filling factor, Q (right-hand column), for reionization histories with $z_r = 6.5$ (top panels) and $z_r = 9.0$ (bottom panels). The solid curve shows the evolution for the linear N_{ion} model, whilst the case of the cubic N_{ion} model is shown by the dashed line. The plotted points represent constraints imposed by values of Γ_{-12} obtained from the Lyα forest opacity by Bolton et al. (2005) and Wyithe & Bolton (2011). The inset in the left-hand panels gives the electron scattering optical depth for the linear and cubic N_{ion} models (τ and $\tau*$, respectively).

filling factor develops more quickly in order to match the electron scattering constraint. Importantly, the two models do provide very different ionization histories at each z_r and therefore should allow us to probe the sensitivity of our temperature predictions to realistic variations in the ionizing background.

4 RESULTS OF THE SEMI-NUMERICAL MODEL

4.1 The IGM thermal state following hydrogen reionization

We now examine the variation of IGM temperature with reionization redshift using the semi-numerical model described in the previous two sections. For any given z_r, and for each of the two different parametrizations of N_{ion}, we compute an optimal N_{ion} evolution that ensures $Q = 1.0$ by z_r. The resulting ionizing background then allows us to calculate the temperature field over the redshift range $5.5 < z < 6.5$, when the quasars analysed in Bolton et al. (2012) are expected to have had their most recent optically-bright phase.

The IGM temperatures predicted by our semi-numerical model at $z = 6.0$ are summarized in Fig. 2. The top two rows display the results using our linear N_{ion} model, for reionization completing by $z_r = 6.5$ (top panels) and $z_r = 9.0$ (bottom panels). The left-hand panels display temperature maps through the centre of the $100 \, h^{-1}$ Mpc simulation volume. The corresponding central panels show maps of the voxel ionization redshifts relative to the redshift at which reionization completes (i.e. $\Delta z = z - z_r$). We note that the structure of ionized bubbles at fixed Δz is very similar for the early and late models. In the case of late reionization, the temperature mimics this ionization structure, with cooler regions centred on the small H II bubbles that were ionized first, and have thus had more time to cool. However, regions of the IGM ionized during the overlap phase retain a clear imprint of heating. The situation is very different for early reionization, where the temperature field shows little correlation with the reionization topology. Instead, the temperature largely reflects the random Gaussian structure of the density field, indicating that even with reionization occurring at $z_r = 9.0$, the temperature has already settled to an almost asymptotic state by $z = 6.0$.

This asymptotic limit is also clear from the temperature–density relation (right-hand panels of Fig. 2). For $z_r = 9.0$, the relation shows an almost power-law dependence with $\gamma - 1 \approx 0.5$ for $T = T_0 \Delta^{\gamma-1}$, characteristic of an asymptotic IGM thermal state which is set by the competition between photoheating and adiabatic cooling (Hui & Gnedin 1997). However, in the case of late reionization, the figure shows much wider 68 per cent confidence limits (dashed curves) below the highest densities, with an inverted power-law slope of $\gamma - 1 \approx -0.2$ for low densities ($\Delta < 1.0$). The scatter and anticorrelation between temperature and density, which arise due to the fact that lower density regions tend to be ionized last allowing them less time to cool, are in qualitative agreement with results from previous numerical and analytical studies (Bolton, Meiksin & White 2004; Trac et al. 2008; Furlanetto & Oh 2009).

The same set of results can also be seen for the cubic model of N_{ion} in the two lower rows in Fig. 2. In this case, the growth of ionized bubbles is significantly different at constant $\Delta z = z - z_r$ for the two reionization redshifts. As described in Section 3.2, late reionization ($z_r = 6.5$) is a more gradual process in this model, with ionization times spread more evenly around the H II bubbles. This has the effect of spreading out the IGM temperatures, so that regions ionized early tend to be cooler. Similarly, the scatter in the temperature–density

relation is increased. On the other hand, for $z_r = 9.0$, reionization is far more rapid, effectively occurring over a redshift interval of $\Delta z = 3.0$. Despite this difference, the temperature field evolves, by $z = 6.0$, to the same asymptotic state as for the linear N_{ion} model (with a slightly reduced scatter in the temperature–density relation due to the more abbreviated differences in ionization time). This reaffirms the conclusion that the thermal memory of hydrogen reionization for $z_r = 9.0$ is largely erased by $z = 6.0$.

To see this more clearly, in Fig. 3 we consider how the mean and standard deviation of the temperature distribution at $z = 6.0$ evolve as a function of reionization redshift. We note that the mean referred to here is not directly comparable to the measurements of Bolton et al. (2012) as it is averaged over the entire density field in the simulation volume and is not simply the temperature at mean density. The results are shown for both the linear (solid red curve) and the cubic (dashed blue curve) N_{ion} models. The mean temperature predicted by the two models only varies by several hundred Kelvin above $z_r \approx 9.0$, and an asymptotic state is fully reached for $z_r \approx 10.5$–11.0. However, for later reionization redshifts, the temperature distributions vary quite rapidly, and for the linear N_{ion} model at $z_r = 6.0$ the IGM is ~ 5000 K hotter than the asymptotic value. This result is slightly more muted for the cubic model, as the elongated reionization history means that large regions of the IGM have longer to cool, thereby reducing the impact of heating on the mean temperature. However, even allowing for this, unit changes in the reionization redshift correspond to temperature variations of up to 1500 K by $z = 6.0$. As this is comparable to the standard deviation of the distributions, changes of $\Delta z_r \approx 1.0$ should be distinguishable on the basis of volume averaged temperature measurements for $z_r < 9.0$, but will require very precise data.

Finally, note that the standard deviation exhibits a minimum at $z_r \sim 7$ for both models, but increases to both lower and higher redshift. At $z_r < 7$, this scatter is driven by the large variation in temperatures resulting from recent, inhomogeneous reionization. In contrast, the scatter at $z_r > 7$ is instead due to the steepening correlation between temperature and density which establishes itself following reionization. Both models asymptotically approach a value of $\sigma(T) \sim 3000$ K for $z_r \gtrsim 10$.

4.2 The temperature in quasar near-zones

Bolton et al. (2012) used the Doppler parameters of H I Lyα absorption lines in the near-zones of seven quasars at $5.8 < z < 6.4$ to measure the IGM temperature at mean density, T_0, within ~ 5 proper Mpc of these sources. In order to compare these observations to our model, we must therefore also include the effect of He II photoheating by the quasars themselves on the IGM temperature.

We calculate this heating as follows. At any given voxel in our simulation volume, we switch on a quasar $t_q = 1.5 \times 10^7$ yr prior to the redshift at which the quasar is observed, and use the procedure outlined in Section 2.5 to calculate the surrounding IGM temperature. We then draw 200 random lines of sight within an ~ 5 proper Mpc region around the quasar, and for each one we measure the temperature–density relation for all voxels. This relation may then be used to infer a temperature at mean density averaged over all 200 lines of sight. Repeating this procedure for 'quasars' centred on all voxels in the simulation box then gives a distribution for the temperatures around a single observed quasar.

In Fig. 4, we show the mean and standard deviation of the simulated temperature distributions *at mean density* for a quasar observed at $z = 6.02$. The results for the mean temperature are displayed for both hard ($\alpha_q = 1.0$, upper curves) and soft ($\alpha_q = 2.0$, lower curves)
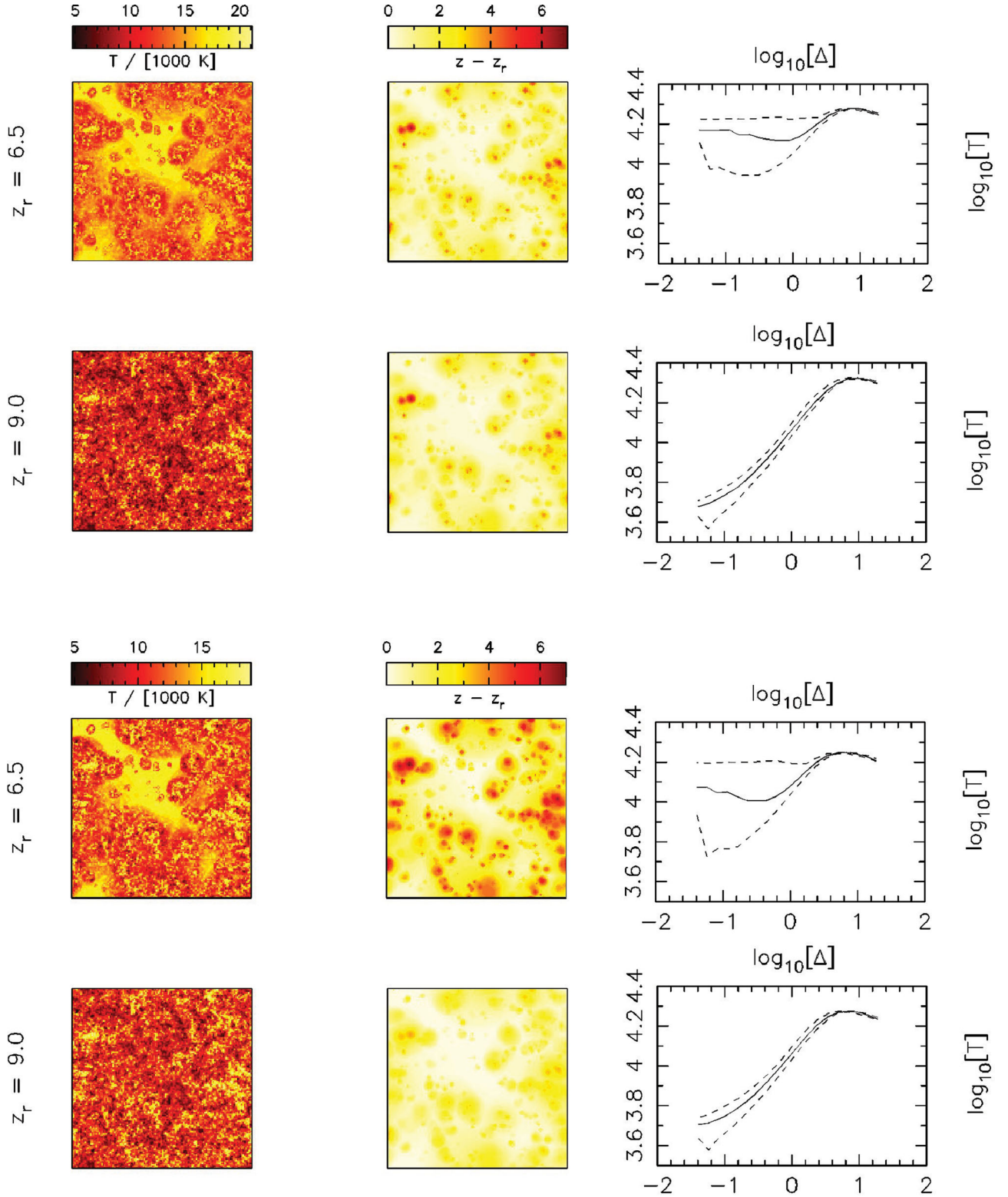
Figure 2. Maps of a two-dimensional slice through the centre of our $100\,h^{-1}$ comoving Mpc simulation box at $z = 6.0$ prior to the inclusion of any quasar heating. The upper six panels show results for the linear $N_{\rm ion}$ model, while the lower set of panels show the same results allowing for the cubic $N_{\rm ion}$ model. In each set, the upper row of panels indicate maps for reionization occurring at $z_{\rm r} = 6.5$ and the lower row for $z_{\rm r} = 9.0$. Left-hand panels: the IGM temperature at the measurement redshift ($z = 6.0$). Middle panels: maps of the ionization redshift for each voxel relative to the redshift at which reionization completes, $\Delta z = z - z_{\rm r}$. Right-hand panels: the IGM temperature, T, against overdensity, Δ, at $z = 6.0$, displaying both the median (solid curve) and 68 per cent intervals around the median (dashed curve).
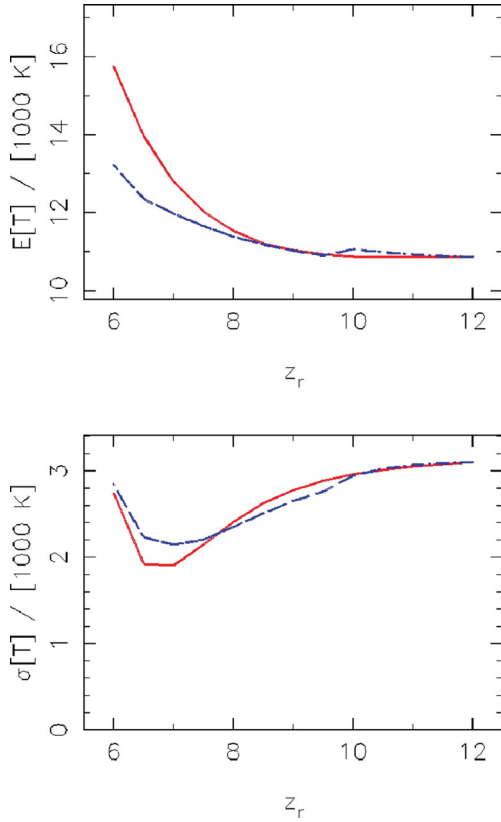
Figure 3. Mean (top panel) and standard deviation (bottom panel) of the simulated temperature distributions at $z = 6.0$ prior to inclusion of quasar heating. Note the results are obtained from the entire $100\,h^{-1}$ comoving Mpc simulation box, and the mean is therefore volume averaged over all densities. We show results for two different cases: the linear N_{ion} model (solid red curves) and the cubic model allowing for an evolving N_{ion} (dashed blue curves).

quasar spectral indices. The red solid and blue dashed curves again correspond to the linear and cubic N_{ion} models, respectively. These retain all the features of the temperature distributions prior to quasar heating, including the asymptotic behaviour of the mean at $z_r \gtrsim 9.0$, and the minimum in the scatter at $z_r \simeq 7.0$. Note, however, the standard deviation tends to be slightly smaller, particularly at large z_r. This is due to the fact that we are now only considering the average temperature at a single (mean) density.

We find that the maximum difference in the average temperature at mean density for the cubic N_{ion} model is only $\sim 2500\,K$ for early and late reionization. Given that the 68 per cent measurement uncertainties on the temperature around individual quasars obtained by Bolton et al. (2012) are ~ 3000–$5000\,K$, it is unlikely that a strong constraint can be obtained from any single line-of-sight observation. However, the combination of all seven quasars analysed by Bolton et al. (2012) reduces the 68 per cent confidence interval on the mean temperature of the quasar near-zones to $\sim 1500\,K$. Therefore, all seven lines of sight will be able, in principle, to distinguish between early and late reionization scenarios.

It is important to note that the rather uncertain quasar spectral index also introduces additional uncertainties into the interpretation of temperature. For example, in the cubic model the temperatures obtained for late reionization combined with a soft quasar spectrum are almost identical to those obtained for early reionization and a much harder quasar spectrum. Unfortunately, there are no direct observations that constrain high-redshift quasar spectral indices,
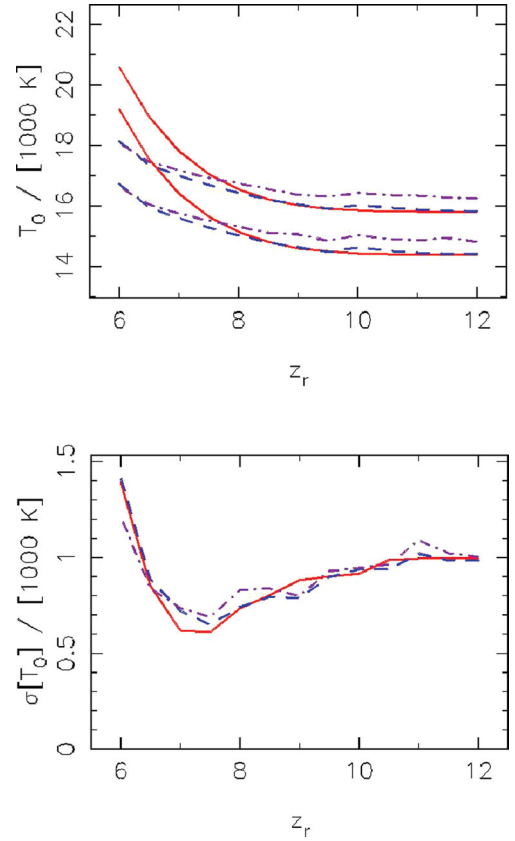

Figure 4. Mean and standard deviation of the simulated distributions over temperature at mean density, $p(T_0|z_r)$, in a quasar proximity-zone at $z = 6.02$. Top panel: simulated mean for three different cases: the linear N_{ion} model (solid curves), the cubic model (dashed curves) and the cubic model accounting for the density bias of quasars (dot–dashed curves). We show simulated temperatures for $\alpha_q = 2.0$, which yield the lower curves and $\alpha_q = 1.0$ giving the higher set of curves. Bottom panel: standard deviations for the aforementioned models. In this case, we only show results for $\alpha_q = 1.0$; however, standard deviations are similar regardless of quasar spectral index.

although a recent study of quasar near-zone sizes at $z \simeq 6$ demonstrated that the range $1.0 \leq \alpha_q \leq 2.0$ is consistent with the data (Wyithe & Bolton 2011). This is in agreement with direct observations at lower redshift (e.g. Telfer et al. 2002), but in practice the quasar spectral index will remain an uncertainty in our analysis.

4.3 Quasar density bias

When calculating the measured temperature distribution expected around the quasars, we have thus far assumed a random distribution of quasar positions in our simulation volume. However, quasars and their host galaxies tend to trace high-density regions owing to the clustering bias of massive haloes. Before calculating the constraints on z_r, we therefore also model the quasar density bias. We weight the temperature distribution calculated in Section 4.2 by the likelihood $\mathcal{L}_g(\delta)$ of observing a quasar at that location

$$p(T|w) = \sum_{\text{all voxels}} \delta(T(x) - T)\mathcal{L}_g(\delta(x)). \qquad (14)$$

The likelihood of observing a galaxy, and a corresponding resident quasar, is then estimated from the Sheth & Tormen (2002) mass

function as

$$\mathcal{L}_g(\delta) = \frac{(1+\delta)\nu(1+\nu^{-2p})e^{-a\nu^2/2}}{\bar{\nu}(1+\bar{\nu}^{-2p})e^{-a\bar{\nu}^2/2}}, \qquad (15)$$

where $\nu = (\delta_c - \delta)/[\sigma(M)]$, $\bar{\nu} = \delta_c/[\sigma(M)]$, and $a = 0.707$ and $p = 0.3$ are constants.

The results including this density bias within the cubic N_{ion} model are shown by the dot–dashed curves in Fig. 4. There is a slight flattening of the temperature differences between different reionization redshifts. This is due to the relatively early reionization time of the high-density regions where quasars are found, which allows them more time to cool to their asymptotic thermal state. At large values of z_r, the temperature is also systematically higher. This is because the higher recombination rate in higher density regions results in slightly larger thermal energy input from photoheating. This increased mean temperature makes it slightly more difficult for measurements of T_0 to differentiate between reionization redshifts. However, this is a minimal effect which will not strongly affect our constraints on z_r.

5 CONSTRAINTS ON THE REIONIZATION HISTORY

In the remainder of this paper, we turn to calculating the constraints that recent and possible future IGM temperature measurements at $z \simeq 6$ impose on the hydrogen reionization redshift. Aside from a number of fixed assumptions including the clumping factor C, star formation mass thresholds M_{min} and M_{ion}, the stellar spectral index α, and the evolution of N_{ion}, there are two critical free parameters in our model, z_r and α_q. For any combination of these two free parameters, we compute mock observations for each z_r and α_q for the ith near-zone temperature measurement, $q^i(z_r, \alpha_q)$. Using Bayes' theorem, we then infer the likelihood for any set of seven independent sight-lines $\{q^i\}_{i=1}^7$ (corresponding to the seven measured temperatures from Bolton et al. 2012):

$$p(\{q^i\}_{i=1}^7|\mathbf{D}, M) = \frac{p(\mathbf{D}|\{q^i\}_{i=1}^7, M)p(\{q^i\}_{i=1}^7|M)}{p(\mathbf{D}|M)}, \qquad (16)$$

where $\mathbf{D}$ is the combination of observational constraints obtained for τ_{CMB}, the ionizing background and the quasar near-zone temperature measurements, M is one of our models for reionization, and $p(\mathbf{D}|M)$ is a normalization constant. The likelihood $p(\mathbf{D}|\{q^i\}_{i=1}^7, M)$ can be easily found from the measured temperature distributions in Fig. 3 and the measured errors on τ_{CMB} (which are taken to be Gaussian) and Γ_{-12}. The prior probability of choosing any set of sight-lines $p(\{q^i\}_{i=1}^7|M)$ is calculated from the density bias likelihood in equation (15) and the assumption that prior information on our free parameters is uniform over the ranges of interest, $1.0 \leq \alpha_q \leq 2.0$ and $6.0 \leq z_r \leq 12.0$. Redshifts outside this range are not considered as they are effectively ruled out at the lower end by the Lyα forest data (Fan et al. 2006) and at the upper end by the measurement of τ_{CMB} (Komatsu et al. 2011).

Using equation (16), we may then find absolute bounds on the reionization redshift by summing over sets of possible sight-lines:

$$p(z_r|\mathbf{D}, M) = \sum_{\{q^i\}} p(\{q^i\}_{i=1}^7|\mathbf{D}, M)\delta(z_r(\{q^i\}_{i=1}^7|M) - z_r), \qquad (17)$$

where the Kronecker delta δ arises since all seven sight-lines are drawn from a single simulation box and correspond to one value of z_r. We note, however, that the same does not hold true for the quasar spectral indices, as each of the individual quasars may have

different intrinsic spectra. Therefore, we only obtain constraints for each quasar spectral index individually:

$$p(\alpha_q^i|\mathbf{D}, M) = \sum_{\{q^i\}} p(\{q^i\}_{i=1}^7|\mathbf{D}, M)\delta(\alpha_q^i(\{q^i\}_{i=1}^7|M) - \alpha_q^i). \qquad (18)$$

Equations (17) and (18) produce model-dependent estimates for our parameters of interest. We note that there are several uncertain aspects of our modelling, which can lead to significant variations in sight-line temperature, particularly for late reionization (Fig. 4).

To both compare the relative probabilities of our different models and obtain a less model-dependent estimate of z_r and α_q^i, we use a Bayesian model comparison to calculate the posterior probability for model M_i, given the data $p(M_i|\mathbf{D})$,

$$p(M_i|\mathbf{D}) = \frac{p(\mathbf{D}|M_i)p(M_i)}{p(\mathbf{D})}. \qquad (19)$$

Here $p(\mathbf{D})$ is again a normalization constant and we assume a priori that all models are equally likely so that $p(M_i)$ is uniform. Model averaging can then be used to infer probabilities of free parameters across all models:

$$p(z_r|\mathbf{D}) = \sum_i p(z_r|\mathbf{D}, M_i)p(M_i|\mathbf{D}), \qquad (20)$$

which provides a more general set of constraints on z_r and α_q^i. These constraints are not completely model-independent as the set of models we consider is not complete. However, as our models bracket most of the physical uncertainties, they should be reliable.

5.1 Reionization constraints from measured near-zone temperatures

In the upper panels of Fig. 5, we present the resulting probability distribution functions over the parameter z_r for the linear N_{ion} model. The distributions are computed for the two different sets of measurements presented by Bolton et al. (2012), derived from their fiducial model (red solid curves) and a model with additional pressure (Jeans) smoothing in the IGM (blue dashed curves). The latter effectively lowers the near-zone temperature constraints by $\sim$3000 K. The upper left-hand panel displays $p(z_r)$ based on the measured values of T_0, τ_{CMB} and Γ_{-12}. For comparison, in the upper right-hand panel we also plot the individual distributions obtained by alternately considering constraints from either τ_{CMB} or T_0 alone combined with our assumed N_{ion} evolution.

As expected, the measurement of T_0 alone does not differentiate between early reionization redshifts, as for all scenarios the IGM has reached an asymptotic temperature. However, the temperature data do provide constraining power for low z_r. We find that irrespective of which set of temperature measurements from Bolton et al. (2012) is considered, very late reionization is ruled out to high confidence. This is because the 5000 K increase in IGM temperature for $z_r < 6.5$ pushes the mean quasar temperature well above the observations.

In the lower panels of Fig. 5, we show corresponding constraints for the cubic model excluding (lower left-hand panel) and including (lower right-hand panel) the effect of quasar density bias. In this model, the observed value of τ_{CMB} is used in defining the parameters governing N_{ion}. It is therefore a much weaker a posteriori constraint and we can no longer rule out reionization at high redshift. Similarly for low z_r, the smaller temperature differences between reionization scenarios means that late reionization cannot be excluded with the same confidence. Furthermore, the relatively tight constraints obtained when considering the temperatures derived assuming a larger Jeans scale are probably not robust, as the
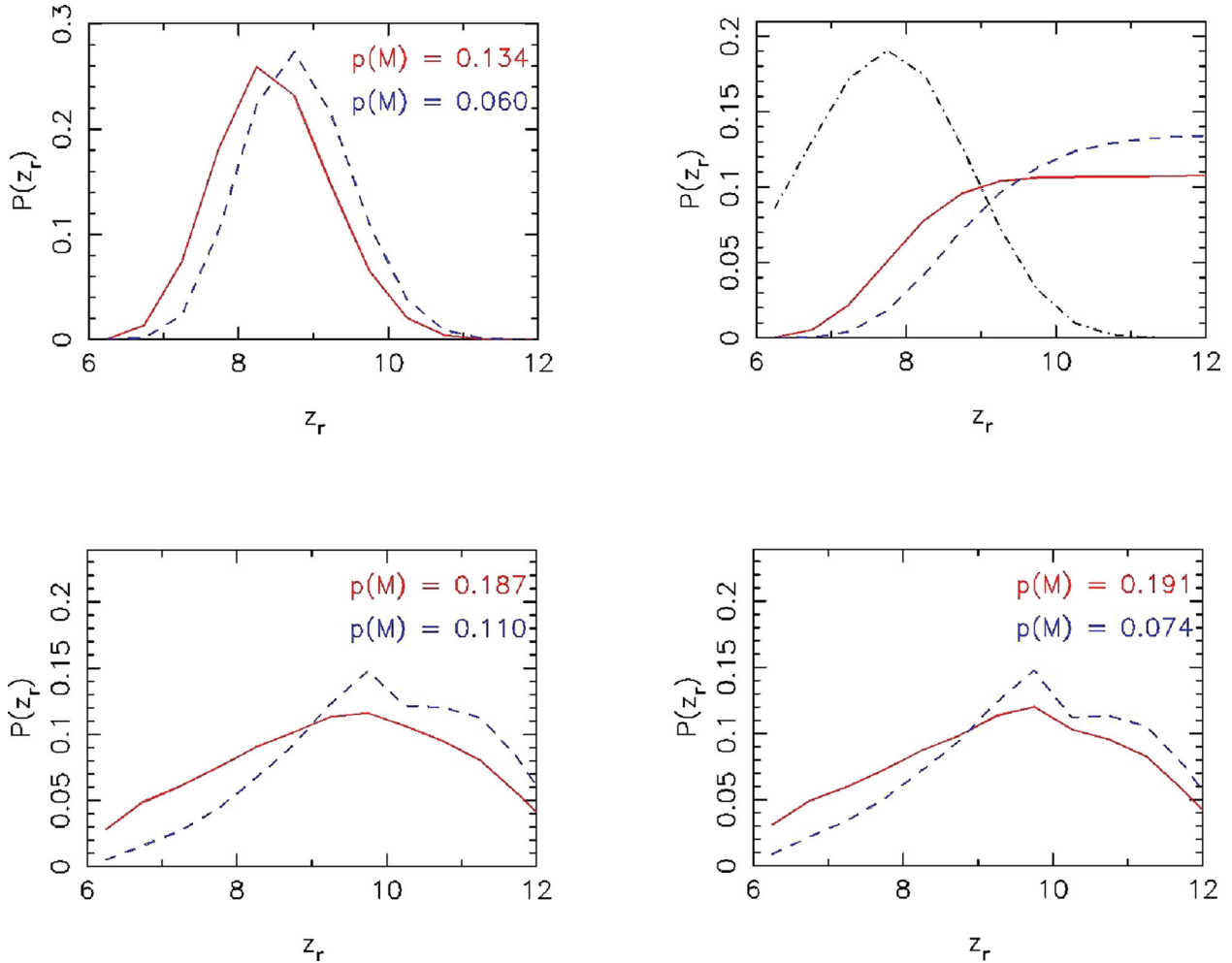
Figure 5. Constraints on reionization redshift based on measured values of T_0, τ_{CMB} and Γ_{-12} for different models of reionization. In each case, two probability distributions are shown, representing constraints from the fiducial near-zone temperature measurements of Bolton et al. (2012) (red solid curves) and allowing for a larger Jeans scale (blue dashed curves). The relative probabilities of each model are shown at the top right-hand corner of each plot. Upper left-hand panel: constraints from T_0 and τ_{CMB} and the linear model for N_{ion}. Upper right-hand panel: constraints obtained from the near-zone temperatures and N_{ion} alone. For comparison, the constraint from τ_{CMB} and N_{ion} alone is shown in the black dot–dashed line. Lower left-hand panel: the probability distributions for the cubic N_{ion} model. Lower right-hand panel: distributions for the cubic model but now accounting for the bias of quasars to regions of high density.

constraints from the fiducial measurements are favoured by a factor of around 3 over these.

The final model averaged distribution is shown in Fig. 6, which corresponds to a mix of the fiducial results from the linear and cubic models. Even though this largely ignores the models with the tightest constraints, we may still conclude that $z_r > 7.9$ (6.5) to 68 (95) per cent confidence. As a sanity check, we also verify that the optimal temperatures predicted by our reionization models match the measurements quite well. Fig. 7 shows the predicted sight-line temperature distributions for the maximum a posteriori estimates of z_r and α_q^i compared to the observed quasar temperatures. We find that although two-thirds of the modelled points lie within the 68 per cent confidence intervals of the observations, the model temperatures of quasars 0 and 1 (following the numbering in Fig. 7) appear to be systematically too high. However, for the fiducial Bolton et al. (2012) measurements this does not provide a strong constraint ruling out our model, since the observed temperature distributions are both positively skewed and broader than Gaussian. Therefore, although our model predictions lie on the edge of the 68 per cent confidence interval, they are only about

a factor of 1.5 less probable than the peak. The same does not hold true for the second set of measurements which account for additional Jeans smoothing. These are ruled out with some significance, which may indicate that the (conservative) systematic error due to additional Jeans smoothing adopted by Bolton et al. (2012) may have been slightly overestimated. The only real outlier then comes from quasar 5 in the fiducial measurements, which is unsurprising since this provides a significantly higher measurement of proximity-zone temperature. This may indicate that a quasar spectral index which is harder than the prior we have assumed (i.e. $\alpha_q < 1$) may be required to reconcile this measurement with the simulations.

It is interesting to contrast this result with recent evidence for a decline in the fraction of Lyman break galaxies that exhibit strong Lyα emission from $z = 5$ to 7 (Ono et al. 2012; Pentericci et al. 2011; Schenker et al. 2011). Assuming the Lyα emission escape fraction does not evolve rapidly, this decline may be attributed to a corresponding decrease in the ionized hydrogen fraction to $Q \approx 0.5$ by $z = 7$, implying reionization finished late. In addition, analyses of the size and shape of the near-zone observed in the spectrum of the
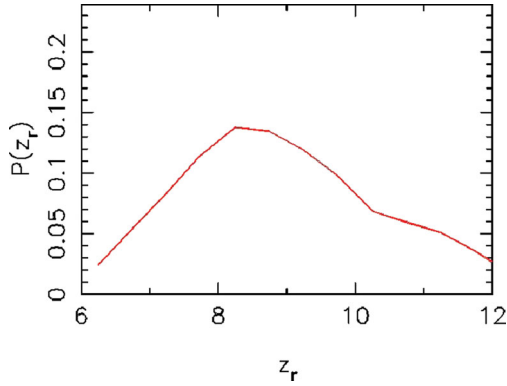
Figure 6. Final constraint on the reionization redshift based on measured values of T_0, τ_{CMB} and Γ_{-12} when averaged over all our different models of reionization. This includes different models for N_{ion}, the bias of quasars to high-density regions and the Jeans pressure smoothing scale. Model averaging significantly weakens constraints as it adds uncertainties to the temperature, but still rules out late reionization to $z_{\mathrm{r}} > 7.9$ (6.5) at 68 (95) per cent confidence.

quasar ULAS J1120+0641 are consistent with $Q \leq 0.9$ at $z \simeq 7.1$ (Bolton et al. 2011; Mortlock et al. 2011), assuming the red damping wing is not due to a proximate high column density absorber. Large neutral fractions of ~ 50 per cent at $z \sim 7$ may be difficult to reconcile with our temperature measurements, which indicate $z_{\mathrm{r}} > 7.9$ (6.5) to 68 (95) per cent. Such large neutral fractions could perhaps be reconciled with our constraint if the average quasar spectral index is much softer than we have assumed, resulting in lower temperatures for a given z_{r} due to less He II photoheating. On the other hand, we note that other possible sources of *hydrogen* reionization, such as Population III stars or mini-quasars, have harder spectra than we consider here. These would therefore tend to increase the heating immediately following reionization. This would then drive IGM temperatures too high to match the Bolton et al. (2012) observations assuming reionization completed late. Consequently, sources which have harder spectra than we have assumed would strengthen rather than weaken our conclusion that late reionization is unlikely.

Similar considerations also apply to uncertainties in the clumping factor C, briefly mentioned in Section 2.1. This is a highly uncertain parameter, whose impact we did not fully model but instead simply assumed to take on a uniform value of $C = 3$. The clumping

factor has an impact on temperature evolution, since increases in clumping factor tend to increase overall recombination, implying more photons are needed to achieve reionization. This results in a corresponding increase in IGM heating of the order of ~ 1000 K for $C = 5$. However, we note that our choice of clumping factor lies at the low end of possible values derived from simulations (Pawlik et al. 2009; Raičević & Theuns 2011). Larger values of the clumping factor should then only rule out late reionization with greater significance for models which have the same z_{r}.

5.2 Prospects for constraints from future temperature measurements

In the previous section, we presented constraints on the reionization redshift from the existing measurements of the IGM temperature around quasars at $z \simeq 6$ (Bolton et al. 2012). This work demonstrates the potential of high-redshift IGM temperature measurements to aid in ruling out very late reionization, so it is therefore interesting to consider if future progress can be made with further data.

We begin by creating mock catalogues of possible future observations. To do this, we assume that for a given z_{r}, ionizing source model and density bias model, N_{obs} observations are to be drawn. For each one, the quasar spectral index is drawn from the uniform prior over α_{q} and the quasars are assumed to have an optically-bright phase which starts at a redshift drawn from uniform distribution in the range $5.8 < z < 6.5$. The median of each new observation is taken at random from our predicted temperature distribution for the chosen z_{r}, the redshift at which the quasar turns on and α_{q}. Finally, the errors in the measurement around this median are assumed to correspond to one of the 14 (seven fiducial and seven augmented Jeans scale) observational measurements chosen at random. Once N_{obs} measurements are drawn in this way for each z_{r} and model, we then use equations (16)–(20) to obtain predicted probability distributions.

This procedure for the generation of mock observations is repeated 100 times, and the resulting distributions are averaged. We then marginalize over the different ionizing source models to obtain a predicted distribution $p(z_{\mathrm{r}})$ for every z_{r} from which the measurements are drawn. This allows us to estimate the confidence with which the reionization redshift can be measured as a function of the true z_{r}. For simplicity, we omit the constraints imposed by τ_{CMB}
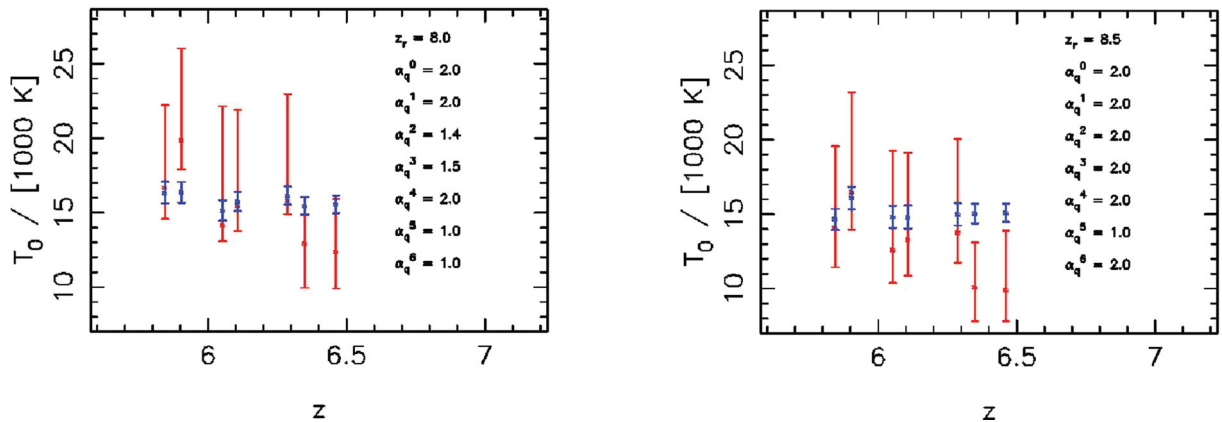
Figure 7. Model averaged quasar temperature distributions at the maximum a posteriori estimate of reionization redshift. We show both the model distributions (blue) and the observed sight-lines (red) with 68 per cent confidence error bars. In both cases, we also include the parameter estimates of z_{r} and α_{q}^0 (rightmost point) through α_{q}^6 (leftmost point). For clarity, we omit redshift ranges and offset observations 3 and 5 by $\Delta z = 0.1$. Left-hand panel: results obtained for the fiducial near-zone temperature measurements. Right-hand panel: results for the measurements with additional Jeans smoothing.
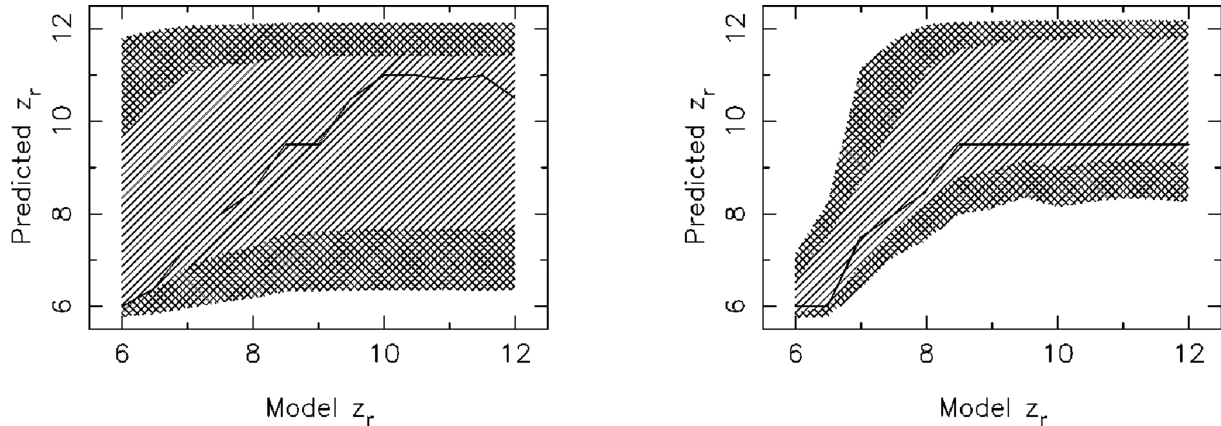
Figure 8. Bias and uncertainty in the constraints on the reionization redshift from near-zone temperatures, as a function of the true reionization redshift in our models. In each case, the mode of the predicted posterior distribution is shown (black line) alongside the 68 per cent (lined region) and 95 per cent (hatched region) confidence intervals. Left-hand panel: results assuming seven near-zone temperature measurements. Right-hand panel: results for 100 near-zone temperature measurements, illustrating the optimistic case of large numbers of quasar sight-lines.

in order to assess the new information drawn from the temperature observations alone.

We present our results in Fig. 8. The left-hand panel shows the mode (solid line) and confidence intervals (filled regions) for $N_{obs} = 7$, mimicking the constraints of the previous section. Meanwhile, the right-hand panel shows the same results for a large number of observations,[1] $N_{obs} = 100$. We note that, in both cases, the mode typically recovers the true reionization redshift in the models well, particularly for small z_r. However, at no reionization redshift do we obtain a particularly tight constraint for seven sight-lines only. For late reionization, this is primarily due to uncertainties in modelling both the quasar spectrum and the ionizing efficiency. Similarly, if reionization happened early, we will not be able to distinguish well between different z_r as the IGM temperature reaches an asymptotic state independent of when reionization occurred. However, increasing the number of observations from 7 to 100 can tighten our constraints on late reionization considerably, increasing the potential 95 per cent limit on z_r from 6.5 to 8.0.

Improved constraints for the average quasar extreme-ultraviolet spectral index from low-redshift data could help to tighten our prior on α_q, and further improve limits at least on late reionization. However, to tighten constraints on early reionization using IGM temperature measurements ultimately requires observations which push to even higher redshifts.

6 CONCLUSIONS

Current understanding of the reionization history is primarily built on existing observational evidence comprised of measurements of the Gunn–Peterson optical depth at $z \lesssim 6$, and the electron scattering optical depth of cosmic microwave photons. These measurements probe, respectively, only the tail end of the epoch of reionization and an integral measure of the reionization history. The available constraints therefore permit a wide range of possible histories. Observa-

tions of the IGM temperature provide an additional complementary probe since the thermal memory of the IGM yields information at redshifts beyond those where observations are made. Measurements of the temperature around high-redshift quasars therefore offer a renewed opportunity to constrain the reionization history of the Universe.

In this paper, we have used measurements of IGM temperature at $z \simeq 6$ (Bolton et al. 2012) to constrain the redshift at which the hydrogen reionization epoch ended. Our analysis employs a semi-numerical model for reionization and heating, which is constrained to fit the CMB electron scattering optical depth, and the ionization rate inferred from the Lyα forest at $z = 6$. We find that all models which reionize the universe prior to $z_r \approx 9.0$ settle to approximately the same IGM thermal state by $z = 6.0$ with relatively little scatter in the temperature at mean density. For late reionization, $(z_r < 8.0)$, the situation is different since there is significantly more variance in the IGM temperature distribution. This arises partly from differences in ionization time, which allow for different cooling times and a greater scatter. However, we find that there is always a detectable thermal imprint of at least 2500 K, which differentiates the mean temperature signifying late reionization, $z_r \approx 6$, from the asymptotic state achieved for $z_r > 9.0$. This implies that measurements of temperature in quasar near-zones can be used to constrain the reionization redshift if it is sufficiently late.

Including observational constraints from the CMB electron scattering optical depth and the Lyα forest opacity, we conclude that $z_r > 7.9$ (6.5) with 68 (95) per cent confidence. The $z \simeq 6$ temperature measurements therefore rule out a very late completion to reionization. Inclusion of further temperature measurements in the future will tighten these constraints. If reionization occurred early, we estimate a sample of 100 quasar spectra would rule out $z_r < 8.0$ to 95 per cent confidence. However, in order to push these constraints further, more detailed modelling of the IGM thermal evolution will also be required. In particular, the evolution of ionizing efficiency with redshift will have to be understood in order to narrow the modelling uncertainties for later reionization scenarios. Including the effect of hydrogen reionization sources which have harder spectra than we have assumed here will also be valuable. Finally, improved estimates of quasar spectral indices will aid in reducing uncertainties in the modelling of the near-zone temperatures.

---

[1] Note that a total of 100 quasar high-resolution spectra at $z \simeq 6$ is a very optimistic scenario. Obtaining one $R \sim 40\,000$ spectrum, even for the brightest known quasars at these redshifts, requires $\sim$10 h of integration on an 8-m class telescope.

REFERENCES

Anninos P., Zhang Y., Abel T., Normal M. L., 1997, New Astron., 2, 209
Barkana R., Loeb A., 2001, Phys. Rep., 349, 125
Becker G. D., Rauch M., Sargent W. L. W., 2007, ApJ, 662, 72
Bolton J. S., Haehnelt M. G., 2007, MNRAS, 374, 493
Bolton J. S., Meiksin A., White M., 2004, MNRAS, 348, L43
Bolton J. S., Haehnelt M. G., Viel M., Springel V., 2005, MNRAS, 357, 1178
Bolton J. S., Oh S. P., Furlanetto S. R., 2009, MNRAS, 395, 736
Bolton J. S., Becker G. D., Wyithe J., Stuart B., Haehnelt M. G., Sargent W. L. W., 2010, MNRAS, 406, 612
Bolton J. S., Haehnelt M. G., Warren S. J., Hewett P. C., Mortlock D. J., Venemans B. P., McMahon R. G., Simpson C., 2011, MNRAS, 416, L70
Bolton J. S., Becker G. D., Raskutti S., Wyithe J., Stuart B., Haehnelt M. G., Sargent W. L. W., 2012, MNRAS, 419, 2880
Bond J. R., Cole S., Efstathiou G., Kaiser N., 1991, ApJ, 379, 440
Carilli C. L. et al., 2010, ApJ, 714, 834
Choudhury T. R., Ferrara A., 2006, MNRAS, 371, L55
Choudhury T. R., Haehnelt M. G., Regan J., 2009, MNRAS, 394, 960
Coles P., Jones B., 1991, MNRAS, 248, 1
Dijkstra M., Haiman Z., Rees M. J., Weinberg D. H., 2004, ApJ, 601, 666
Eisenstein D. J., Hu W., 1999, ApJ, 511, 5
Fan X. et al., 2006, ApJ, 132, 117
Faucher-Giguère C.-A., Lidz A., Zaldarriaga M., Hernquist L., 2009, ApJ, 703, 1416
Furlanetto S. R., Oh S. P., 2008, ApJ, 681, 1
Furlanetto S. R., Oh S. P., 2009, ApJ, 701, 94
Geil P. M., Wyithe J., Stuart B., 2008, MNRAS, 386, 1683
Gnedin N. Y., Fan X., 2006, ApJ, 648, 1
Haiman Z., Loeb A., 1997, ApJ, 483, 21
Hu E. M., Kim T.-S., Cowie L. L., Songaila A., Rauch M., 1995, AJ, 110, 1526
Hui L., Gnedin N. Y., 1997, MNRAS, 292, 27
Hui L., Haiman Z., 2003, ApJ, 596, 9
Komatsu E. et al., 2011, ApJS, 192, 18
Madau P., Meiksin A., 1994, ApJ, 433, L53
Mesinger A., 2010, MNRAS, 407, 1328
Mesinger A., Furlanetto S., 2007, ApJ, 669, 663
Miralda Escudé J., 2003, ApJ, 597, 66
Misawa T., Tytler D., Iye M., Kirkman D., Suzuki N., Lubin D., Kashikawa N., 2007, AJ, 134, 1634
Mitra S., Choudhury T. R., Ferrara A., 2011, MNRAS, 413, 1569
Mortlock D. J. et al., 2011, Nat, 474, 616
Ono Y. et al., 2012, ApJ, 744, 83
Pawlik A. H, Schaye J., van Scherpenzeel E., 2009, MNRAS, 394, 1812
Pentericci L. et al., 2011, ApJ, 743, 132
Petitjean P., Webb J. K., Rauch M., Carsell R. F., Lanzetta K., 1993, MNRAS, 262, 499
Pritchard J. R., Loeb A., Wyithe J. Stuart B., 2010, MNRAS, 408, 57
Raičević M., Theuns T., 2011, MNRAS, 412, L16
Schenker M. A., Stark D. P., Ellis R. S., Robertson B. E., Dunlop J. S., McLure R. J., Kneib J.-P., Richard J., 2012, ApJ, 744, 179
Sheth R. K., Tormen G., 2002, MNRAS, 329, 61
Songaila A., Cowie L. L., 2010, ApJ, 721, 1448
Telfer R. C., Zheng W., Kriss G. A., Davidsen A. F., 2002, ApJ, 565, 773
Theuns T., Schaye J., Zaroubi S., Kim T. S., Tzanavaris P., Carswell B., 2002, ApJ, 567, L103
Thomas R. M. et al., 2009, MNRAS, 393, 32
Trac H., Cen R., Loeb A., 2008, ApJ, 689, L81
Verner D. A., Ferland G. J., Korista K. T., Yakovlev D. G., 1996, ApJ, 465, 487
White R. L., Becker R. H., Fan X., Strauss M. A., 2003, AJ, 126, 1
Wyithe J. Stuart B., Bolton J. S., 2011, MNRAS, 412, 1926
Wyithe J. Stuart B., Loeb A., 2003, ApJ, 586, 693
Wyithe J. Stuart B., Loeb A., 2007, MNRAS, 375, 1034
Wyithe J. Stuart B, Hopkins A. M., Kistler M. D., Yuksel H., Beacom J. F., 2010, MNRAS, 401, 2561
Zahn O., Lidz A., McQuinn M., Dutta S., Hernquist L., Zaldarriaga M., Furlanetto S. R., 2007, ApJ, 654, 12
Zaldarriaga M., Hui L., Tegmark M., 2001, ApJ, 557, 519

This paper has been typeset from a TEX/LATEX file prepared by the author.